Direct Simulations of Breaking Ocean Waves with Data Assimilation

Douglas G. Dommermuth, Lucas E. Rhymes, and James W. Rottman
Science Applications International Corporation
10260 Campus Point Drive
San Diego, California 92121
Email:douglas.g.dommermuth@saic.com, lucas.e.rhymes@saic.com,
and james.w.rottman@saic.com

***Abstract*—The Numerical Flow Analysis (NFA) code is modified to assimilate data from lower bandwidth High-Order Spectral (HOS) simulations. NFA is a Cartesian-based LES code with Volume of Fluid (VOF) interface capturing. HOS is used to nudge the lowest wavenumber content in the NFA assimilation, and the highest wavenumbers are estimated to investigate the effects of wave nonlinearity and wave breaking. The formulation can be generalized to assimilate radar measurements of the ocean surface.**

I. Introduction

Three-dimensional numerical simulations of phased-resolved ocean waves are primarily limited to single-valued free surfaces with wave slopes no greater than one. Examples include the High-Order Spectral (HOS) method that is described in [1]. HOS is a potential-flow method with no capability to model turbulence or wave overturning. Unlike HOS, NFA provides the capability to simulate wave breaking directly including the effects of turbulence. Data assimilation has been used in HOS (see [2], [3], and [4]). However, HOS realizations of ocean waves have limited bandwidth. In contrast, NFA is specifically designed to fill in the high wavenumber portion of the wave spectrum that cannot be measured simultaneously with the long waves.

As noted by [5] in their annual review paper on breaking waves in deep and intermediate waters, as investigators "chip away at the difficult problem of quantifying wave breaking through laboratory investigations, field measurements, and numerical simulations, it is likely that progress will continue at a very slow pace." What [5] fail to recognize is the impact that modern VOF methods in combination with data assimilation and supercomputers will have on understanding the effects of wave breaking. The authors of [5] state that "At this juncture, direct numerical simulations are not a viable option for ocean wave calculations over a large domain; therefore, a simpler approach should be adopted to model the breaking effects." As we show in this paper, the authors are mistaken. Modern VOF methods with data assimilation implemented on today's supercomputers can resolve wave breaking over large patches of the ocean surface.

As an example, figure 1 shows ray traced images of the free surface produced by NFA from data assimilations of HOS realizations based on the JONSWAP and Pierson-Moskowitz ocean spectra. The wave breaking in the JONSWAP assimilation is more vigorous than the Pierson-Moskowitz assimilation. The electronic versions of this paper can be magnified to inspect the wave spilling that is ocurring.

II. Formulation

In this section we describe the NFA numerical algorithms and the assimilation of HOS simulations into NFA. The HOS algorithm used in this paper is a slightly modified version of the algorithm described in [1].

A. Governing Equations

Consider the immiscible turbulent flow at the interface between air and water with ρ_a and ρ_w respectively denoting the densities of air and water. Similar to the potential-flow approaches, physical quantities are normalized by characteristic velocity (U_o), length (L_o), time (L_o/U_o), density (ρ_w), and pressure ($\rho_w U_o^2$) scales.

Let α denote the fraction of fluid that is inside a cell. By definition, $\alpha = 0$ for a cell that is totally filled with air, and $\alpha = 1$ for a cell that is totally filled with water. In terms of α, the normalized density is expressed as

$$\rho(\alpha) \quad = \quad \lambda + (1-\lambda)\alpha \ , \tag{1}$$

where $\lambda = \rho_a/\rho_w$ is the density ratio between air and water.

Let u_i denote the normalized three-dimensional velocity field as a function of normalized space (x_i) and normalized time (t). The conservation of mass is

$$\frac{\partial \rho}{\partial t} + \frac{\partial u_j \rho}{\partial x_j} = 0 \ . \tag{2}$$

For incompressible flow,

$$\frac{\partial \rho}{\partial t} + u_j \frac{\partial \rho}{\partial x_j} = 0 \ . \tag{3}$$

Subtracting Equation (3) from (2) gives a solenoidal condition for the velocity:

$$\frac{\partial u_i}{\partial x_i} = 0 \ . \tag{4}$$

Substituting Equation (1) into (2) and making use of (4), provides an advection equation for the volume fraction:

$$\frac{\partial \alpha}{\partial t} + \frac{\partial}{\partial x_j}(u_j \alpha) = 0 \ . \tag{5}$$

978-0-933957-40-4 ©2013 MTS

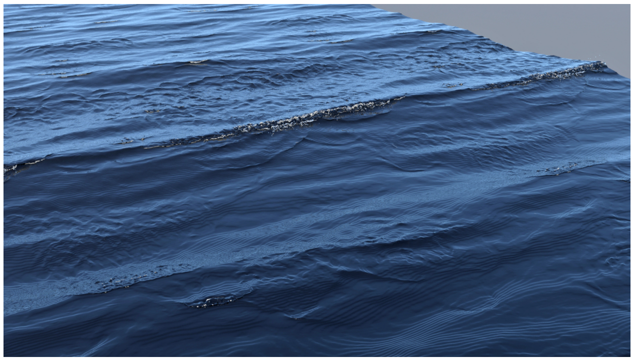

(a)

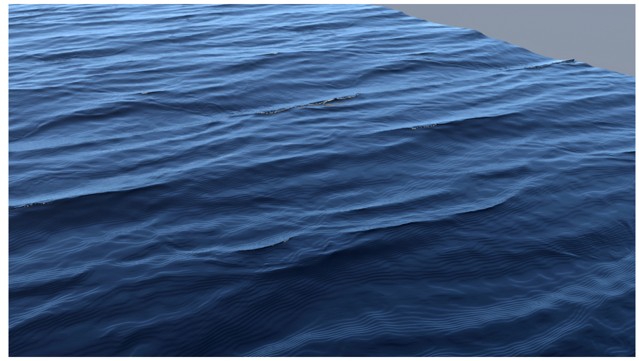

(b)

Fig. 1. Ray traced images of the free surface. (a) JONSWAP assimilation. (b) Pierson-Moskowitz assimilation.

For an infinite Reynolds number, viscous stresses are negligible, and the conservation of momentum is

$$\frac{\partial u_i}{\partial t} + \frac{\partial}{\partial x_j}\left(u_j u_i\right) = -\frac{1}{\rho}\frac{\partial p}{\partial x_i} - \frac{p_s}{\rho}\frac{\partial H(\alpha)}{\partial x_i} - \frac{\delta_{i3}}{F_r^2} \quad , \tag{6}$$

where $F_r^2 = U_o^2/(gL_o)$ is the Froude number, and g is the acceleration of gravity. p is the pressure and p_s is a stress that acts normal to the interface. $H(\alpha)$ is a Heaviside function, and δ_{ij} is the Kronecker delta function.

The divergence of the momentum equations (6) in combination with the solenoidal condition (4) provides a Poisson equation for the dynamic pressure:

$$\frac{\partial}{\partial x_i}\frac{1}{\rho}\frac{\partial p}{\partial x_i} = \Sigma \quad , \tag{7}$$

where Σ is a source term. The pressure is used to project the velocity onto a solenoidal field. Details of the volume fraction advection, the pressure projection, and the numerical time integration are provided in [6] and [7]. Sub-grid scale stresses are modeled using an implicit model that is built into the treatment of convective terms.

B. NFA Smoothing

The free-surface boundary layer is not resolved in VOF simulations at high Reynolds numbers with large density jumps such as air and water. Under these circumstances, the tangential velocity is discontinuous across the free-surface interface and the normal component is continuous. As a result, unphysical tearing of the free surface tends to occur. Favre-like filtering can be used to alleviate this problem by forcing the air velocity at the interface to be driven by the water velocity in a physical manner. Consider the following projection,

$$\tilde{u}_i = \begin{cases} \langle \rho u_i \rangle / \langle \rho \rangle & \text{for } \alpha \leq 0.5 \\ u_i & \text{for } \alpha > 0.5 \end{cases} \quad , \tag{8}$$

where $\tilde{u}_i$ is the smoothed velocity field, u_i is the unfiltered velocity field, ρ is the density, and α is the volume fraction. Brackets denote smoothing.

$$\langle F(\mathbf{x}) \rangle = \int_{\mathrm{v}_\xi} W(\mathbf{x}_\xi) F(\mathbf{x} - \mathbf{x}_\xi) \mathrm{dv}_\xi \quad . \tag{9}$$

Here, $F(x)$ is a general function, v is a control volume that surrounds a cell, and $W(x)$ is a weighting function that neither overshoots or undershoots the maximum or minimum allowable density. Due to the high density ratio between water and air, equation 8 tends to push the water-particle velocity into the air. Once the velocity is filtered, we need to project it back onto a solenoidal field in the fluid volume (V).

$$u_i = \tilde{u}_i - \frac{1}{\rho}\frac{\partial \psi}{\partial x_i} \ \text{ in V} \ , \tag{10}$$

where ψ is a potential function. For an incompressible flow, we require that u_i is solenoidal care of Equation (4). Substituting (10) into (4) gives a Poisson equation for ψ:

$$\frac{\partial}{\partial x_i}\frac{1}{\rho}\frac{\partial \psi}{\partial x_i} = \frac{\partial \tilde{u}_i}{\partial x_i} \ \text{ in V} \ . \tag{11}$$

We typically apply the filtering every 20 to 80 time steps. Details of the implementation of the preceding filter are provided in [8].

C. NFA Time Integration

Based on [9], a second-order Runge-Kutta scheme is used to integrate with respect to time the field equations for the velocity field. Here, we illustrate how a volume of fluid formulation is used to advance the volume-fraction function. Similar examples are provided by [10]. During the first stage of the Runge-Kutta algorithm, a Poisson equation for the pressure is solved:

$$\frac{\partial}{\partial x_i}\frac{1}{\rho(\alpha^k)}\frac{\partial P^*}{\partial x_i} = \frac{\partial}{\partial x_i}\left(\frac{u_i^k}{\Delta t} + R_i\right) \quad , \tag{12}$$

where R_i denotes the nonlinear convective, hydrostatic, and atmospheric forcing terms in the momentum equations. u_i^k and ρ^k are respectively the velocity components at time step k. Δt is the time step. P^* is the first prediction for the pressure field.

For the next step, this pressure is used to project the velocity onto a solenoidal field. The first prediction for the velocity field (u_i^*) is

$$u_i^* = u_i^k + \Delta t\left(R_i - \frac{1}{\rho(\alpha^k)}\frac{\partial P^*}{\partial x_i}\right) \quad . \tag{13}$$

The volume fraction is advanced using a volume of fluid operator (VOF):

$$\alpha^* = \alpha^k - \mathrm{VOF}\left(u_i^k, \alpha^k, \Delta t\right) \quad . \tag{14}$$

A Poisson equation for the pressure is solved again during the second stage of the Runge-Kutta algorithm:

$$\frac{\partial}{\partial x_i}\frac{1}{\rho(\alpha^*)}\frac{\partial P^{k+1}}{\partial x_i} = \frac{\partial}{\partial x_i}\left(\frac{u_i^* + u_i^k}{\Delta t} + R_i\right) \quad . \tag{15}$$

u_i is advanced to the next step to complete one cycle of the Runge-Kutta algorithm:

$$u_i^{k+1} = \frac{1}{2}\left(u_i^* + u_i^k + \Delta t\left(R_i - \frac{1}{\rho(\alpha^*)}\frac{\partial P^{k+1}}{\partial x_i}\right)\right) \quad , \tag{16}$$

and the volume fraction is advanced to complete the algorithm:

$$\alpha^{k+1} = \alpha^k - \mathrm{VOF}\left(\frac{u_i^* + u_i^k}{2}, \alpha^k, \Delta t\right) \quad . \tag{17}$$

In NFA, the free surface is reconstructed from the volume fractions using piece-wise linear polynomials. The reconstruction is based on algorithms that are described by [11]. The surface normals are estimated using weighted central differencing of the volume fractions. A similar algorithm is described by [12]. The advection portion of the algorithm is operator split, and it is based on similar algorithms reported in [13]. One difference between the present algorithm and earlier methods includes a special treatment to alleviate mass-conservation errors due to the presence of non-solenoidal velocity fields.

Let F_i denote the flux through the faces of a cell:

$$F_i = A_i u_i \quad . \tag{18}$$

A_i correspond to the surface areas that bound the cell. Based on an application of Gauss's theorem to the volume integral of equation 2 and making use of equation 4:

$$F_i^+ - F_i^- = 0 \quad , \tag{19}$$

where F_i^+ is the flux on the positive i-th face of the cell and F_i^- is the flux on the negative i-th face of the cell. Due to numerical errors, equation 19 is not necessarily satisfied. Let $\mathcal{E}$ denote the resulting numerical error for any given cell. For each cell whose flux is not conserved, a correction is applied prior to performing the VOF advection. For example, the following reassignment of the flux along the vertical direction ensures that the redefined flux is conserved:

$$\begin{aligned} \tilde{F}_3^+ &= F_3^+ - \frac{\mathcal{E}}{2} \\ \tilde{F}_3^- &= F_3^- + \frac{\mathcal{E}}{2} \quad . \end{aligned} \tag{20}$$

Based on this new flux, new face velocities are defined on the faces of the cell:

$$\tilde{u}_i = \frac{\tilde{F}_i}{A_i} \quad . \tag{21}$$

Equation 5 is operator split. A dilation term is added to ensure that the volume fraction remains between $0 \leq \alpha \leq 1$ during each stage of the splitting [13], [14]. The resulting discrete set of equations for the first stage of the Runge-Kutta time-stepping procedure is provided below:

$$\begin{aligned} \alpha^{(1)} = \alpha^k \quad &- \quad \frac{\mathcal{F}_1\left[\left(u_1^+\right)^k, \alpha^k, \Delta t\right] - \mathcal{F}_1\left[\left(u_1^-\right)^k, \alpha^k, \Delta t\right]}{\mathrm{V}} \\ &+ \quad \Delta t\, c_c \frac{\left(u_1^+\right)^k - \left(u_1^-\right)^k}{\Delta x_1} \\ \alpha^{(2)} = \alpha^{(1)} \quad &- \quad \frac{\mathcal{F}_2\left[\left(u_2^+\right)^k, \alpha^{(1)}, \Delta t\right] - \mathcal{F}_2\left[\left(u_2^-\right)^k, \alpha^{(1)}, \Delta t\right]}{\mathrm{V}} \\ &+ \quad \Delta t\, c_c \frac{\left(u_2^+\right)^k - \left(u_2^-\right)^k}{\Delta x_2} \\ \alpha^* = \alpha^{(2)} \quad &- \quad \frac{\mathcal{F}_3\left[\left(\tilde{u}_3^+\right)^k, \alpha^{(2)}, \Delta t\right] - \mathcal{F}_3\left[\left(\tilde{u}_3^-\right)^k, \alpha^{(2)}, \Delta t\right]}{\mathrm{V}} \\ &+ \quad \Delta t\, c_c \frac{\left(\tilde{u}_3^+\right)^k - \left(\tilde{u}_3^-\right)^k}{\Delta x_3} \quad , \end{aligned} \tag{22}$$

$\mathcal{F}_i$ denotes VOF advection along the cartesian axes, $\mathrm{V} = \Delta x_1 \Delta x_2 \Delta x_3$ is the volume of the cell, and c_c is an coefficient that is designed to conserve flux and prevent overfilling or under filling of a cell [14]:

$$c_c = \begin{cases} 1 & \text{for } 0.5 \leq \alpha^k \leq 1 \\ 0 & \text{for } 0 < \alpha^k \leq 0.5 \end{cases} \quad . \tag{23}$$

Note that the order of the operator splitting is alternated from time step to time step to preserve second-order accuracy and to prevent any biasing.

D. Seaway Representation

Pierson-Moskowitz and JONSWAP spectrums are used to initialize simulations of seaways. The wavelength at the peak of the spectrum (L_o) is used to normalize length scales. The velocity scale is $U_o = \sqrt{gL_o}$. Based on these choices for L_o and U_o, the Froude number equals one ($F_r = 1$). In normalized variables, the one-dimensional Pierson-Moskowitz spectrum in wavenumber space is

$$S_{\mathrm{PM}}(k) = \frac{\alpha_p}{2k^3}\exp\left(-\frac{3}{2}\left(\frac{k_o}{k}\right)^2\right) \quad , \tag{24}$$

where $\alpha_p = 8.1 \times 10^{-3}$ is Phillips' constant. Similarly, the JONSWAP spectrum is

$$S_{\mathrm{J}}(k) = \frac{\alpha_p}{2k^3}\exp\left(-\frac{5}{4}\left(\frac{k_o}{k}\right)^2\right)\gamma^a \quad , \tag{25}$$

where γ controls the height of the spectral density relative to a Pierson-Moskowitz spectrum and

$$a = \exp\left(-\frac{1}{2}\left(\frac{\sqrt{k} - \sqrt{k_o}}{\sigma_a\sqrt{k_o}}\right)^2\right) \quad . \tag{26}$$

σ_a controls the widths of the left and right sides of the spectrum as follows:

$$\sigma_a = \begin{cases} 0.07, & k < k_o \\ 0.09, & k \geq k_o \end{cases} \quad . \tag{27}$$

A cosine spreading function is used to simulate a directional spectrum.

$$D(\theta) = \frac{1}{2\sqrt{\pi}}\frac{\Gamma(s+1)}{\Gamma(s+\frac{1}{2})}\cos^{2s}\left(\frac{1}{2}(\theta - \theta_o)\right) \quad , \tag{28}$$

where s controls the amount of spreading and θ_o is the primary direction of the waves. Γ is the Gamma function.

E. Data Assimilation

As illustrated in Figure 2, data is sequentially assimilated into NFA every N time steps. Here, we illustrate the assimilation of HOS simulations into NFA. The procedure can be generalized to assimilate radar data into NFA. HOS, like radar measurements, is bandwidth limited. In the case of HOS, approximations, including the Taylor series approximation, the perturbation expansion, and the single-valued free surface, limit the relative difference of the maximum wavenumber to the wavenumber at the peak of spectrum to about two decades. Radar measurements over a patch of the ocean surface have similar resolution limitations. HOS simulations or radar measurements are assimilated into NFA to drive the lowest wavenumbers in the NFA simulation, and the highest wavenumbers in the NFA simulation are estimated to enable modeling of wave breaking. In the NFA data assimilation, energy cascades down from the lowest wavenumbers to the highest wavenumbers through the action of nonlinear wave interactions where it is dissipated due the effects of wave breaking.

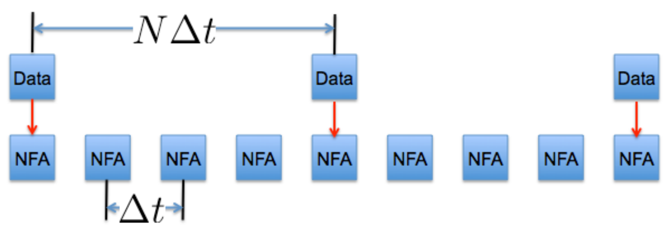

Fig. 2. Sequential Assimilation.

The HOS formulation is based on irrotational flow, i.e. the wavy portion of the flow. Depending on the type, radar measures the position of the ocean surface or the velocities on the ocean surface, which can be directly related to the wavy portion of the flow. NFA models the wavy and the vortical portions of the flow. Under these circumstances, the framework for assimilating HOS and radar data into NFA drives only the wavy portion of the flow while letting the vortical portion of the flow to freely evolve. A separation of the flow into wavy and vortical components is similar to the Helmholtz decomposition that is used by [15] in his studies of the interaction of a vortex pair with a free surface.

A properly posed free-surface problem requires the assimilation of two surface quantities for the wavy portion of the flow. We assimilate the free-surface elevation and the normal component of velocity evaluated on the free surface. As discussed earlier, these two quantities are assimilated differently depending on whether the wavenumber k is above or below a cutoff wavenumber k_c. The incremental changes in the free-surface elevation ($\Delta\eta$) and the normal velocity (Δu_n) are

$$\Delta\eta = \Delta\eta^L + \Delta\eta^H \tag{29}$$
$$\Delta u_n = \Delta u_n^L + \Delta u_n^H \ , \tag{30}$$

where the superscript L and H symbols denote low pass and high pass filtering, respectively. As shown in §II-G, incremental changes at low wave numbers are assimilated using a nudging technique. As shown in §II-H, incremental changes at high wave numbers are estimated based on theoretical considerations of a saturated wave spectrum.

The change in the free-surface elevation is added to the old free-surface elevation to get the new position of the free surface:

$$\eta^{\mathrm{NEW}} = \eta^{\mathrm{OLD}} + \Delta\eta \ . \tag{31}$$

As shown in §II-I, the change in the free-surface elevation is also used to update the volume fraction:

$$\alpha^{\mathrm{NEW}} = U(\alpha^{\mathrm{OLD}}, \Delta\eta) \ , \tag{32}$$

where U is a function that preserves overturning waves, bubbles, and droplets that may be present in the volume fraction.

The change in the normal component of velocity evaluated on the free surface is used to calculate new velocities throughout the entire domain:

$$u_i^{\mathrm{NEW}} = u_i^{\mathrm{OLD}} + \mathcal{P}(\Delta u_n) \ , \tag{33}$$

where $\mathcal{P}$ is a projection operator that is described in §II-J.

F. Transfer Functions

The volume fraction and water-particle velocities as calculated by NFA are not suitable for the assimilation of data. As shown in [16], height functions provided the best agreement between NFA predictions and experimental measurements of turbulent roughening of the free surface behind the transom stern of a model-scale ship.

We define the free surface in terms of height functions expressed in terms of the volume fraction. The calculation is performed in three steps. First, we define a height function integrating the volume fraction from the bottom of the computational domain to the top and subtract out the water depth. This provides an initial estimate of the free-surface elevation η_1:

$$\eta_1(x,y,t) = \int_{-d}^{h} dz\alpha(x,y,z,t) - d \ , \tag{34}$$

where d is the water depth, h is the height of the air, and α is the volume fraction. Then the air pockets that are trapped beneath η_1 are added back to provide a water column without bubbles.

$$\eta_2(x,y,t) = \eta_1(x,y,t) + \int_{-d}^{\eta_1(x,y,t)} dz(1-\alpha(x,y,z,t)) \ . \tag{35}$$

Finally, the droplets above η_2 are subtracted out to provide a water column without bubbles and without droplets.

$$\eta^{\mathrm{NFA}}(x,y,t) = \eta_2(x,y,t) - \int_{\eta_2(x,y,t)}^{h} dz\alpha(x,y,z,t) \ . \tag{36}$$

We evaluate the surface water-particle velocities as predicted by NFA on η^{NFA}.

$$u_i^s(x,y,t) = u_i|_{z=\eta^{\mathrm{NFA}}} \ . \tag{37}$$

We define a unit normal n_i that points into the air in terms of the height function η^{NFA}. Then the normal component of velocity evaluated on the position of the free surface predicted by NFA is

$$u_n^{\mathrm{NFA}}(x,y,t) = u_i^s n_i^{\mathrm{NFA}} \ . \tag{38}$$

G. Incremental Changes at Low Wave Numbers

For $k \le k_c$, the NFA free-surface elevations and the NFA normal component of velocity on the free surface are nudged toward their HOS counterparts as follows:

$$\begin{aligned} \Delta\eta^L &= -\beta N \Delta t(\eta^{\rm NFA} - \eta^{\rm HOS})^L && (39) \\ \Delta u_n^L &= -\beta N \Delta t(u_n^{\rm NFA} - u_n^{\rm HOS})^L \ , && (40) \end{aligned}$$

where $\beta = O(1)$ is a relaxation factor and recall that N is the number of time steps between injections. $\eta^{\rm HOS}$ is the position of the free surface as predicted by HOS, and $u_n^{\rm HOS}$ is the corresponding normal component of velocity. In the context of Equations 31 and 33, the differences between the NFA predictions and the HOS simulations as represented in the preceding equations are used to nudge the NFA predictions toward the HOS results for low wave numbers, $k \le k_c$.

As a model of nudging, consider following difference equation:

$$\varphi^{n+1} = \varphi^n - \beta N \Delta t(\varphi^n - \varphi^*) \ , \tag{41}$$

where n denotes the number of the injection, φ^{n+1} is the *new* variable, φ^n is the *old* variable, and φ^* is the target variable. The general solution of 41 is

$$\varphi^n = (\varphi^o - \varphi^*)(1 - \beta N \Delta t)^n + \varphi^* \ , \tag{42}$$

where φ^o is the initial variable. As $n \to \infty$, $\varphi^n \to \varphi^*$, i.e. the target, as long as $\beta N \Delta t < 1$. As formulated, the difference between the current value of φ^n and the target value φ^* is used to nudge φ toward the target solution.

H. Incremental Changes at High Wave Numbers

For $k > k_c$, the spectral densities of the free-surface elevation and normal velocity are calculated in the NFA data assimilation using the height function 36 and the normal component of velocity evaluated on the height function 38. We denote these spectral densities of the free-surface elevation and the normal velocity by $S_\eta(k)$ and $S_u(k)$, respectively.

For a fully saturated spectrum as $k \to \infty$, the spectral density of the free-surface elevation behaves as

$$S_{\eta_o}(k) \to \frac{\alpha_p}{2k^3} \ . \tag{43}$$

Similarly, the spectral density of the normal velocity on the free surface behaves as

$$S_{u_o}(k) \to \frac{\alpha_p}{2k^2} \ . \tag{44}$$

Due to the effects of wave breaking and numerical dissipation, the wave energy in the NFA assimilation will decay between injections. We increase the energy in the NFA assimilation at high wave numbers in a manner that is similar to the pumping that is used in the HOS simulations [17].

In wave number space, for $k > k_c$, we rescale the modal amplitudes of the free-surface elevation and normal velocity as follows:

$$\begin{aligned} \widetilde{\Delta\eta^H} &= f_\eta(k)\widetilde{\eta^{\rm NFA}} && (45) \\ \widetilde{\Delta u_n^H} &= f_u(k)\widetilde{u_n^{\rm NFA}} \ , && (46) \end{aligned}$$

where the tilde symbol denotes a Fourier transform in wave number space, and f_η and $f_u(k)$ are real factors that do not change the phases of the short-scale waves. In terms of the spectral densities, the scaling factors are

$$\begin{aligned} f_\eta(k) &= \sqrt{\frac{S_{\eta_o}(k)}{S_\eta(k)}} - 1 && (47) \\ f_u(k) &= \sqrt{\frac{S_{u_o}(k)}{S_u(k)}} - 1 \ . && (48) \end{aligned}$$

We further limit the maximum allowable change that can occur at high wave numbers by enforcing $|f_\eta| \le f_{\max}$ and $|f_u| \le f_{\max}$. We typically set $f_{\max} = 0.2$

I. Total Free-Surface Increment

The increment in the free-surface elevation needs to be converted into a change in the volume fraction. The conversion should preserve any wave overturning that is present in the old volume fraction. The change in the free-surface elevation is used to update the volume fraction by defining a pseudo velocity:

$$W(x,y,z) = \frac{\Delta\eta(x,y)}{\tau} \ , \tag{49}$$

where $\Delta\eta(x,y)$ is the free-surface increment and τ is a pseudo time.

The resulting pseudo velocity W is constant in time and along the z axis. Based on a Courant constraint, a pseudo time step is chosen such that $\Delta\tau < \min(\Delta z)/\max(W)$, where Δz is the grid spacing along the z axis. Setting $\tau = 1$, we let $\Delta\tau = 1/N_\tau$, where here N_τ is an integer such that $N_\tau > \max(\Delta\eta)/\min(\Delta z)$.

The volume fraction is updated by integrating the following equation:

$$\frac{\partial\alpha}{\partial\tau} + \frac{\partial W\alpha}{\partial z} = 0 \ , \tag{50}$$

where at $\tau = 0$, $\alpha = \alpha^{\rm OLD}$.

Similar to Equation 22, VOF reconstruction and advection are used to integrate the preceding equation in N_τ steps:

$$\alpha^{\rm n+1} = \alpha^n - \frac{\mathcal{F}_3\left[W, \alpha^n, \Delta\tau\right] - \mathcal{F}_3\left[W, \alpha^n, \Delta\tau\right]}{\rm V} \quad n = 0, \ldots, N_\tau, \tag{51}$$

where $\alpha^0 = \alpha^{\rm OLD}$ and $\alpha^{\rm NEW} = \alpha^N$.

J. Total Velocity Increment

The increment in the normal component of velocity evaluated on the position of the free surface is used to provide an Neumann condition for a projection operator. Since the wavy portion of the flow is irrotational, we define velocity potentials in the water and air that are respectively denoted by $\phi^{\rm H_2O}$ and $\phi^{\rm AIR}$. The following boundary-value problem is solved in the water:

$$\begin{aligned} \nabla^2\phi^{\rm H_2O} &= 0 \ \text{for} \ -d \le z \le \eta^{\rm NEW} \\ \frac{\partial\phi^{\rm H_2O}}{\partial n} &= \Delta u_n \ \text{on} \ z = \eta^{\rm NEW} \\ \frac{\partial\phi^{\rm H_2O}}{\partial z} &= 0 \ \text{on} \ z = -d \ . && (52) \end{aligned}$$

Here, $\vec{n}$ is the unit normal to η^{NEW} that points from the water into the air. Similarly, the boundary-value problem in the air is

$$\begin{aligned}\nabla^2\phi^{\mathrm{Air}} &= 0 \ \text{ for } \ \eta^{\mathrm{NEW}} \le z \le h \\ \frac{\partial\phi}{\partial n}^{\mathrm{Air}} &= \Delta u_n \ \text{ on } \ z = \eta^{\mathrm{NEW}} \\ \frac{\partial\phi}{\partial z}^{\mathrm{Air}} &= 0 \ \text{ on } \ z = h \ .\end{aligned} \tag{53}$$

Equations 52 and 53 are solved using the method of fractional areas. Details associated with the calculation of the area fractions are provided in [18] along with additional references.

Given the velocity potentials in the water and air, the velocity increment is projected down into the water and up into the air as follows:

$$u_i^{\mathrm{NEW}} = u_i^{\mathrm{OLD}} + \begin{cases} \frac{\partial\phi}{\partial x_i}^{\mathrm{H_2O}} & -d \le z \le \eta^{\mathrm{NEW}} \\ \frac{\partial\phi}{\partial x_i}^{\mathrm{Air}} & \eta^{\mathrm{NEW}} \le z \le h \end{cases} \ . \tag{54}$$

As constructed, the normal component of the velocity increment across the air-water interface is continuous whereas the tangential component is discontinuous. The density-weighted velocity smoothing that is discussed in §II-B mitigates this effect.

III. Results

A. HOS Studies

We first illustrate the capabilities of our HOS code. We consider simulations of short-crested seas using HOS to study the effects of perturbations in phase and amplitude. The simulations are initialized using a JONSWAP spectrum with a peak enhancement factor $\gamma = 6$ and with a slight angular spreading as specified by $s = 50$ and $\theta_o = 0$ (see Equations 25-28). The significant wave height is $H_s = 0.03664$, which is 1.566 times greater than the corresponding Pierson-Moskowitz spectrum. The HOS simulation is three dimensional with $N_x \times N_y = 1024 \times 1024 = 1,048,576$ de-alaised Fourier modes. The HOS uses a fourth-order approximation. The length (L), width (W), and depth (d) of the HOS simulation are respectively 20, 20, and 10 in normalized units. The HOS simulations are run for 65,000 time steps with $\Delta t = 0.001$. The period of adjustment of the HOS is $T_o = 20$ [19]. Smoothing is used every time step throughout the HOS simulation. The energy is pumped to maintain constant total energy, and the linear portions of the free-surface boundary conditions are integrated analytically. The ratio of the maximum resolved wavenumber (k_{M}), which includes the effects of smoothing, to the wavenumber at the peak of the spectrum is $k_{\mathrm{M}}/(2\pi) = 92.16$, which is over five times greater than the bandwidth reported by [20] in their studies of rogue waves due to modulation instabilities.

The effect of perturbations on the statistics of the free-surface elevation are investigated by making small changes the to the wave phase and wave amplitude. The perturbations are added at time $t = 40$ after the waves have had sufficient time to adjust. The random perturbations in phase are formulated as follows:

$$\begin{aligned}(\tilde{\eta}_{ij})^{\mathrm{NEW}} &= (\tilde{\eta}_{ij})^{\mathrm{OLD}} \exp(\imath\theta_{ij}) \\ (\tilde{\phi}^s_{ij})^{\mathrm{NEW}} &= (\tilde{\phi}^s_{ij})^{\mathrm{OLD}} \exp(\imath\theta_{ij}) \ ,\end{aligned} \tag{55}$$

where θ_{ij} is uniformly distributed between $\pm 2\pi\theta$ with $\theta = 0.05$. $\tilde{\eta}$ and $\tilde{\phi}^s$ are the Fourier modes of the free-surface elevation and the surface potential, respectively. The random perturbations in amplitude are

$$\begin{aligned}(\tilde{\eta}_{ij})^{\mathrm{NEW}} &= (\tilde{\eta}_{ij})^{\mathrm{OLD}}(1 + a_{ij}) \\ (\tilde{\phi}^s_{ij})^{\mathrm{NEW}} &= (\tilde{\phi}^s_{ij})^{\mathrm{OLD}}(1 + a_{ij}) \ ,\end{aligned} \tag{56}$$

where a_{ij} is uniformly distributed between $\pm a$ with $a = 0.05$.

Figure 3 shows the kurtosis of the free-surface elevation for the three cases. The change in the kurtosis is greater for changes in phase than it is for changes in amplitude. The maximum kurtosis is comparable to those observed in [20]. The changes in the kurtosis due to perturbations in phase occur over a much shorter time scale than the modulation instabilities that are investigated in [20]. Granted the phase changes that we induce occur instantaneously, but we think that changes in wave phase could occur quickly in nature under the action of currents, changes in wind speed and direction, bottom topography, and merging of wave systems. Figure 4 shows probability distributions for surface elevation for the three cases compared with Gaussian theory. The probability distribution is averaged over time for $63 \le t \le 65$. The probability distributions are asymmetrical because the wave crests are sharper than the wave troughs due to second-order Stokes effects. The crest extrema are greatest for the phase perturbations. The wave crests are higher than those reported in [20] who used a much larger domain, albeit with less bandwidth.

Nonlinear waves are sensitive to phase especially near the crests of long waves where short waves steepen [21]. Nonlinear waves are also susceptible to crest instabilities that can lead to wave breaking [22]. For sufficiently steep waves, waves whose phases are in alignment will break. As the sea state matures, with no interactions that could lead to changes in phase, the waves that are left are those waves whose phases are not in alignment, which is a particular type of equilibrium. With respect to the formation of rogue waves, [20] show the limitations of the second-order theory of [23], but the Stokes expansion that is used in [23] does not permit changes in phase due to wave interactions. Second-order wave theories that properly account for phase may be useful for studying the formation of rogue waves over time scales that are much shorter than the modulation instabilities that are studied in [20]. As this study shows, the effects of non-equilibrium on the formation of extreme events is important.

B. NFA Studies

NFA is adapted to HOS simulations of Pierson-Moskowitz (24) and JONSWAP (25-27) spectrums to study the effects of wave breaking for short-crested seas. The peak enhancement factor is $\gamma = 6$ for the JONSWAP spectrum. The angular spreading is $s = 50$ with $\theta_o = 0$ (28). The significant wave heights for the JONSWAP and Pierson-Moskowitz spectrums are $H_s = 0.036638$ and 0.02339, respectively. The HOS simulations use $N_x \times N_y = 256 \times 64 = 16,384$ de-alaised Fourier modes. The HOS simulations use fourth-order approximations. The length (L), width (W), and depth (d) of the HOS simulations are respectively 5, 1.25, and 0.5 in normalized units. The periods of adjustment are $T_o = 10$.

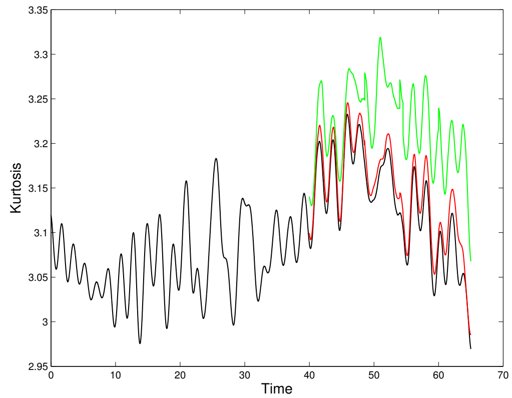

Fig. 3. Kurtosis of free-surface elevation. Base case: (————). Amplitude perturbation: (————). Phase perturbation: (————).

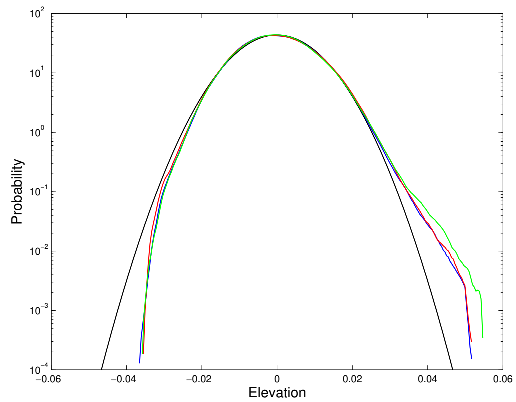

Fig. 4. Probability distribution of free-surface elevation. Gaussian theory: (————). Base case: (————). Amplitude perturbation: (————). Phase perturbation: (————).

The HOS simulations are initially run with large time steps during the adjustment phase. Once the free surfaces have been adjusted, the HOS simulations are run for 85,000 time steps with $\Delta t = 0.000625$. The time steps are very small to facilitate assimilation into NFA. The HOS simulations are smoothed every time step, and each HOS simulation uses energy pumping to maintain the total energy.

The lengths (L), widths (W), depths of water (d), and heights of air (h) of the NFA simulations are respectively 5, 1.25, 0.5, and 0.5. The numbers of grid points along the x, y, and z-axes are respectively 4096, 1024, and 512 for each simulation. The total number of grid points for each simulation is approximately 2.15 billion grid points. The grid spacings are constant along the x and y-axes with $\Delta x = \Delta y = 0.0012207$. The grid spacings are clustered along the z-axes near $z = 0$. The minimum grid spacing along the z-axis is $\Delta z = 0.001123$ for each simulation. The time steps of the NFA simulations are $\Delta t = 0.000625$. The HOS simulations are injected into the NFA simulations every $N = 80$ time steps. The HOS data is assimilated for wave numbers $k_c \leq 70$ (see Equations 39-40). The relaxation factor is $\beta = 2$ for each simulation. The HOS simulations are assimilated after the HOS has been adjusted and before the HOS show local maxima in the Kurtosis, which corresponds to time $t = 34.375$ in the HOS. Higher wave number content is estimated based on a saturated spectrum (see Equations 43-48). The data assimilations are run for over 32,000 time steps.

Figures 5 and 6 show respectively the probability distributions and spectral densities of the free-surface elevations for the JONSWAP and Pierson-Moskowitz data assimilations. The results for the NFA assimilations are time-averaged between $0 \leq t \leq 20$. The plots of probability include the theoretical distributions based on Gaussian theory. The plots of spectral density include the theoretical spectra.

For the probability distributions in figure 5, the higher resolution of the NFA assimilations relative to the HOS simulations leads to higher wave crests and shallower troughs. The waves are steeper in the NFA assimilations than they are in the HOS simulations. The differences between NFA and HOS are greatest for the JONSWAP case, which has more nonlinearity, less Gaussian behavior, and more wave breaking than the Pierson-Moskowitz case. We note that the limited domain size limits the extrema that are observed in the probability distributions of both assimilations.

The spectral densities in figure 6, show the higher resolution that is present in NFA relative to HOS. The NFA bandwidth is about 20 times greater than the HOS. The HOS simulations show a slight energy pileup for wave numbers $k > k_c$. The NFA spectral densities, which are calculated just prior to injection, dip for wave numbers slightly above $k = k_c$ and then rise for wave numbers $k \approx 700$. This effect could be due to wave breaking moving wave energy from low to high wave numbers. The differences between the theoretical spectra and the numerical results at low wave numbers are due to the limited domain sizes and the resulting low sampling rates.

Figures 7 and 8 show respectively the skewness and kurtosis of the free-surface elevations for the JONSWAP and Pierson-Moskowitz data assimilations in comparison to HOS. The plots of skewness indicate that the NFA data assimilations have higher crests and shallower troughs than the HOS simulations. The kurtoses of NFA and HOS closely track each other with the greatest differences occurring near the maxima, but unlike the skewnesses, there is no clear trend for one to be greater than the other. The differences between the NFA and HOS statistics are reduced as the assimilations mature and equilibrate under the action of wave breaking as discussed in §III-A. We note that there is still wave breaking toward the ends of the assimilations, but the breaking is more gentle with less high extrema than the breaking that occurrs at the beginnings of the assimilations.

Figure 9 shows wave cuts of the JONSWAP and Pierson-Moskowitz data assimilations compared to HOS for different instants of times. The JONSWAP assimilation shows a very strong plunging breaking wave for $5. \leq t \leq 5.25$ at equal intervals. The tip of the plunging breaking wave is flipped backward. This is due to the jump in the tangential component of velocity that occurs across the free-surface interface. As shown in [24], more frequent applications of density-weighted velocity smoothing is used to remedy this problem. The Pierson-Moskowitz assimilation shows a spilling breaking wave for $6. \leq t \leq 6.25$ at equal intervals. The NFA results closely follow the HOS results except at the wave crests where plunging and spilling occurs.

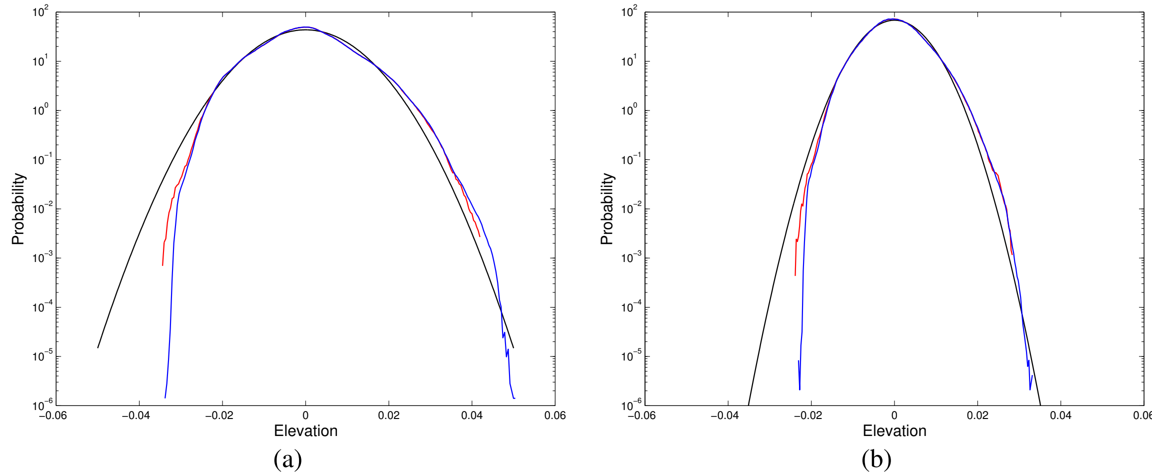

Fig. 5. Probability distribution of free-surface elevation. (a) JONSWAP assimilation. (b) Pierson-Moskowitz assimilation. Theory: (———). HOS: (———). NFA: (———).

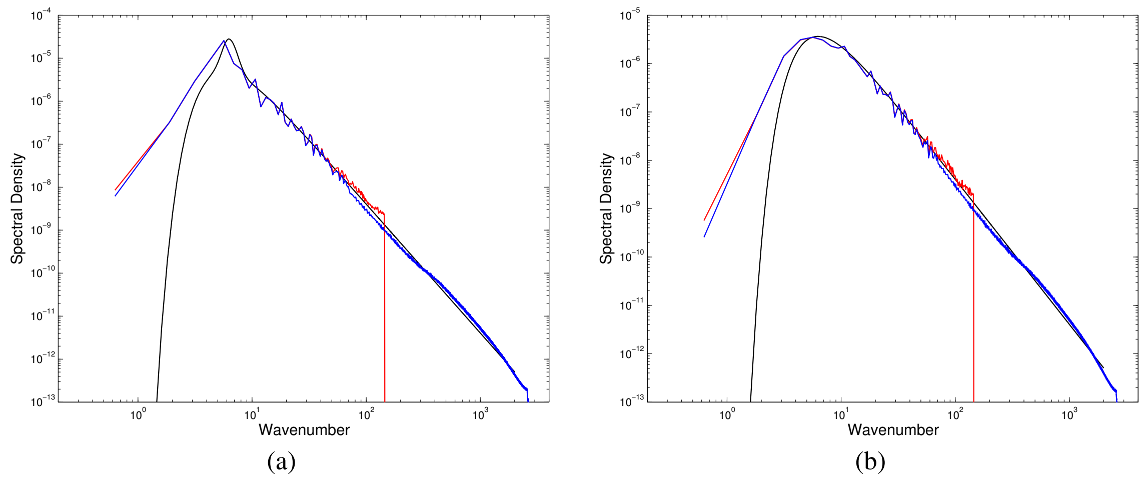

Fig. 6. Spectral density of free-surface elevation. (a) JONSWAP assimilation. (b) Pierson-Moskowitz assimilation. Theory: (———). HOS: (———). NFA: (———).

IV. Conclusion

A formulation for assimilating data into NFA has been developed. The data assimilation is illustrated by injecting HOS simulations into NFA. The process is also applicable to the assimilation of radar measurements of the ocean surface. The low wavenumber portion of the wave spectrum is assimilated using nudging, and high wavenumbers are estimated. The assimilation of data into NFA permits the investigation of higher bandwidths than is possible using either HOS simulations or field measurements. Since the irrotational portion of the flow is assimilated and the vortical flow is free to evolve, the data assimilation allows the investigation of turbulent flows that are not possible using either HOS or field measurements of the ocean surface. NFA models wave breaking that cannot be modeled using HOS. Direct simulations of wave breaking using NFA allow a more detailed analysis of ocean-wave physics than is possible using remote sensing of the ocean surface. Future plans include performing data assimilations of larger patches of the ocean surface with higher resolution to investigate the statistics and underlying structure of breaking waves.

Acknowledgment

This research was sponsored by Dr. Thomas Drake at the Office of Naval Research (contract number N00014-12-C-0568). The numerical simulations were supported in part by a grant from the Department of Defense High Performance Computing Modernization Program (http://www.hpcmo.hpc.mil/). The numerical simulations were performed on the SGI ICE X at the U.S. Air Force Research Laboratory and the IBM iDataPlex at the Navy DoD Supercomputing Resource Center. We thank Richard Walters, Christopher Lewis, and Miguel Valenciano at the Data Analysis Assessment Center of the U.S. Army Engineer Research and Development Center for the ray-traced free-surface visualization used in figure 1. We are grateful to Dr. Charles Linwood Vincent and Dr. Robert Hall for their helpful suggestions. Animated versions of the numerical simulations described here as well as many others are available online at http://www.youtube.com/waveanimations.

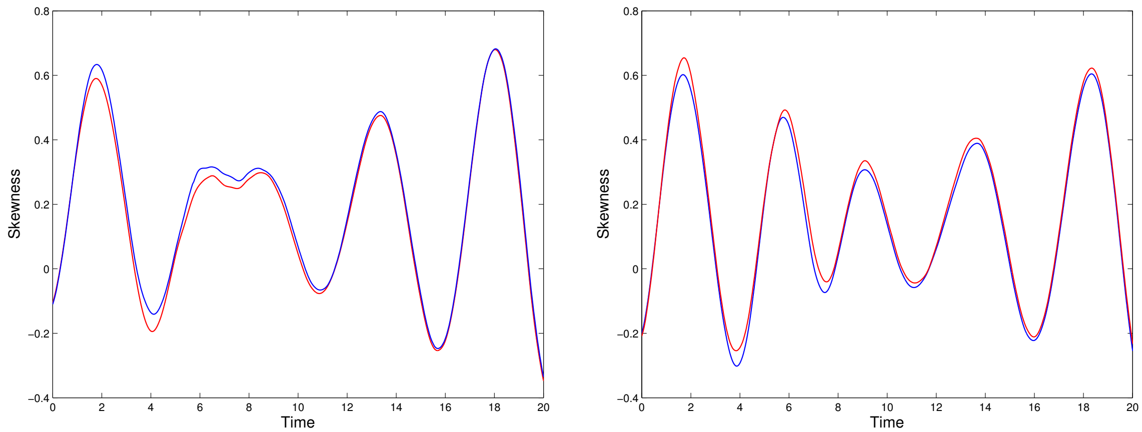

(a) (b)

Fig. 7. Skewness of free-surface elevation. (a) JONSWAP assimilation. (b) Pierson-Moskowitz assimilation. HOS: ( ). NFA: ( ).

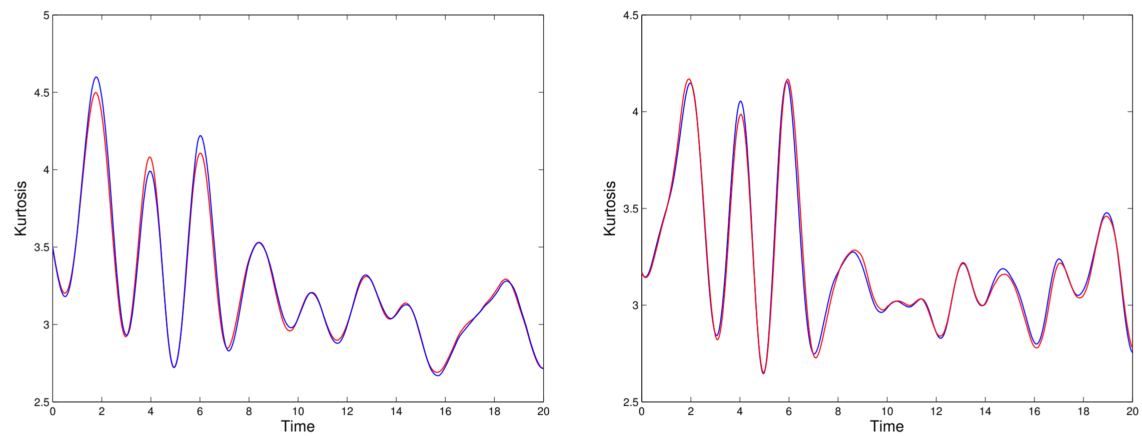

(a) (b)

Fig. 8. Kurtosis of free-surface elevation. (a) JONSWAP assimilation. (b) Pierson-Moskowitz assimilation. HOS: ( ). NFA: ( ).

REFERENCES

[1] D. G. Dommermuth and D. K. Yue, "A high-order spectral method for the study of nonlinear gravity waves," *J. Fluid Mech.*, vol. 187, pp. 267–288, 1987.

[2] G. Wu, "Direct simulation and deterministic prediction of large-scale nonlinear ocean wave field," Ph.D. dissertation, MIT, 2004.

[3] S. Hassanaliaragh, "Radar data assimilation and forecasts of evolving nonlinear wave fields," Ph.D. dissertation, University of Michigan, 2009.

[4] E. Blondel, F. Bonnefoy, and P. Ferrant, "Deterministic non-linear wave predition using probe data," *Ocean Engineering*, vol. 37, pp. 913–926, 2010.

[5] M. Perlin, W. Choi, and Z. Tian, "Breaking waves in deep and intermediate waters," *Ann. Rev. Fluid Mech.*, vol. 45, pp. 115–145, 2013.

[6] D. G. Dommermuth, T. T. O'Shea, D. C. Wyatt, T. Ratcliffe, G. D. Weymouth, K. L. Hendrikson, D. K. Yue, M. Sussman, P. Adams, and M. Valenciano, "An application of cartesian-grid and volume-of-fluid methods to numerical ship hydrodynamics," in *Proceedings of the 9th International Conference on Numerical Ship Hydrodynamics*, Ann Arbor, Michigan, 2007.

[7] T. T. O'Shea, K. A. Brucker, D. G. Dommermuth, and D. C. Wyatt, "A numerical formulation for simulating free-surface hydrodynamics," in *Proceedings of the 27th Symposium on Naval Hydrodynamics*, Seoul, Korea, 2008.

[8] T. C. Fu, T. Ratcliffe, T. T. O'Shea, K. A. Brucker, R. S. Graham, D. C. Wyatt, and D. G. Dommermuth, "A comparison of experimental measurements and computational predictions of a deep-v planing hull," in *Proceedings of the 28th Symposium on Naval Hydrodynamics*, Pasadena, California, USA, 2010, to appear.

[9] M. Sussman, "A second order coupled level set and volume-of-fluid method for computing growth and collapse of vapor bubbles," *J. Comp. Phys.*, vol. 187, pp. 110–136, 2003a.

[10] W. Rider, D. Kothe, S. Mosso, J. Cerutti, and J. Hochstein, "Accurate solution algorithms for incompressible multiphase flows," *AIAA paper 95–0699*, 1994.

[11] D. Gueyffier, J. Li, A. Nadim, R. Scardovelli, and S. Zaleski, "Volume-of-fluid interface tracking with smoothed surface stress methods for three-dimensional flows," *J. Comp. Phys.*, vol. 152, pp. 423–456, 1999.

[12] J. Pilliod and E. Puckett, "Second-order accurate volume-of-fluid algorithms for tracking material interfaces," Lawrence Berkeley National Laboratory, Technical Report LBNL–40744, 1997.

[13] E. Puckett, A. Almgren, J. Bell, D. Marcus, and W. Rider, "A second-order projection method for tracking fluid interfaces in variable density incompressible flows," *J. Comp. Physics*, vol. 130, pp. 269–282, 1997.

[14] G. Weymouth and D.-P. Yue, "Conservative volume-of-fluid method for free-surface simulations on cartesian grids," *J. Comp. Phys.*, vol. 229, no. 8, pp. 2853–2865, 2010.

[15] D. G. Dommermuth, "The laminar interactions of a pair of vortex tubes with a free surface," *J. Fluid Mech.*, vol. 246, pp. 91–115, 1993.

[16] D. A. Drazen, A. M. Fullerton, T. C. Fu, K. L. Beale, T. T. O'Shea, K. A. Brucker, D. C. Wyatt, S. Bhushan, P. M. Carrica, and F. Stern,

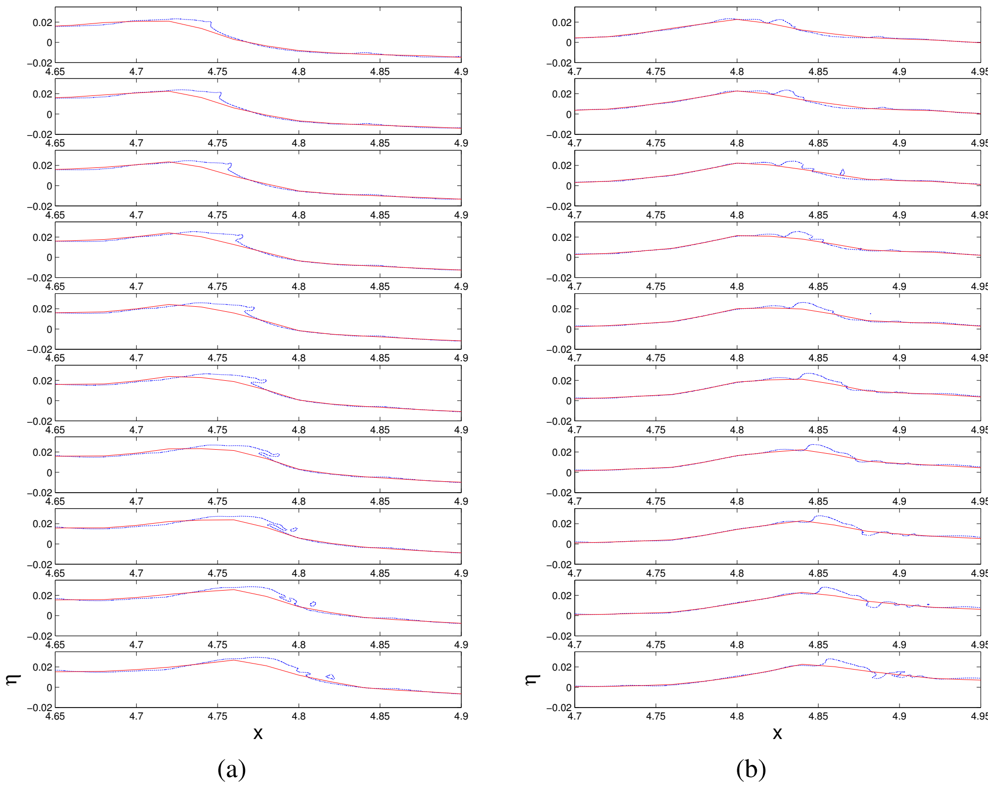

Fig. 9. Wave cuts of the free surface. (a) JONSWAP assimilation. (b) Pierson-Moskowitz assimilation. HOS: (————). NFA: (————).

"Comparisons of model-scale experimental measurements and computational predictions for the transom wave of a large-scale transom model," in *Proceedings of the 28th Symposium on Naval Hydrodynamics*, Pasadena, California, USA, 2010, to appear.

[17] D. G. Dommermuth, T. C. Fu, T. T. O'Shea, K. A. Brucker, and D. C. Wyatt, "Numerical prediction of a seaway," in *Proceedings of the 28th Symposium on Naval Hydrodynamics*, Pasadena, California, USA, 2010, to appear.

[18] M. Sussman and D. Dommermuth, "The numerical simulation of ship waves using cartesian-grid methods," in *Proceedings of the 23rd Symposium on Naval Ship Hydrodynamics*, Nantes, France, 2001, pp. 762–779.

[19] D. G. Dommermuth, "The initialization of nonlinear waves using an adjustment scheme," *Wave Motion*, vol. 32, pp. 307–317, 2000.

[20] W. Xiao, Y. Liu, G. Wu., and D.-P. Yue, "Rogue wave occurrence and dynamics by direct simulations of nonlinear wave-field evolution," *J. Fluid Mech.*, vol. 720, pp. 357–392, 2013.

[21] M. Longuet-Higgins and R. Stewart, "Changes in the form of short gravity waves on long waves and tidal currents," *J. Fluid Mech.*, vol. 8, pp. 565–583, 1960.

[22] M. Longuet-Higgins and D. Dommermuth, "Crest instabilities of gravity waves. part 3. nonlinear development and breaking," *J. Fluid Mech.*, vol. 336, pp. 33–50, 1997.

[23] M. Tayfun, "Narrow-band nonlinear sea waves," *J. Geophys. Res*, vol. 85, no. C3, pp. 1548–1552, 1980.

[24] K. A. Brucker, T. T. O'Shea, D. G. Dommermuth, and P. Adams, "Numerical simulations of breaking waves – weak spilling to strong plunging," in *Proceedings of the 28th Symposium on Naval Hydrodynamics*, Pasadena, California, USA, 2010, to appear.